Article

Isolation of relaxation times under open-circuit conditions: Toward prognosis of nascent short circuits in Li-ion batteries

Rest Period or Open Circuit Voltage (OCV) is characterized by a 2 stage relaxation:

$$OCV = Ae^{(-t/\tau_1)} + Be^{(-t/\tau_2)}$$

1. **Short Tail:** Removal of flux leads to solid phase diffusion induced equilibration inside the electrode particles, the time scale, τ_1 of which is ~ Radius²/Diffusivity and also depends on the temperature, state of charge, ageing extent etc.

2. **Long Tail:** relaxation is sensitive to the presence of leakage currents due to a short circuit and thus, τ_2 can be used to detect and measure short circuits:

Thus: Short Resistance, $R_{sh} = f(^{\tau}2)$

Sagar Bharathraj,
Myeongjae Lee,
Shashishekar P.
Adiga, K.
Subramanya
Mayya, Jin-Ho Kim

s.bharathraj@samsung.com
(S.B.)
shashi.adiga@samsung.com
(S.P.A.)

Highlights
Rest-period voltage is derived to be a double-exponential model with two time constants

The long-term time constant (τ_2) is sensitive to short circuit-linked leakage currents

Tracking τ_2 leads to early-stage short circuit detection and accurate severity estimation

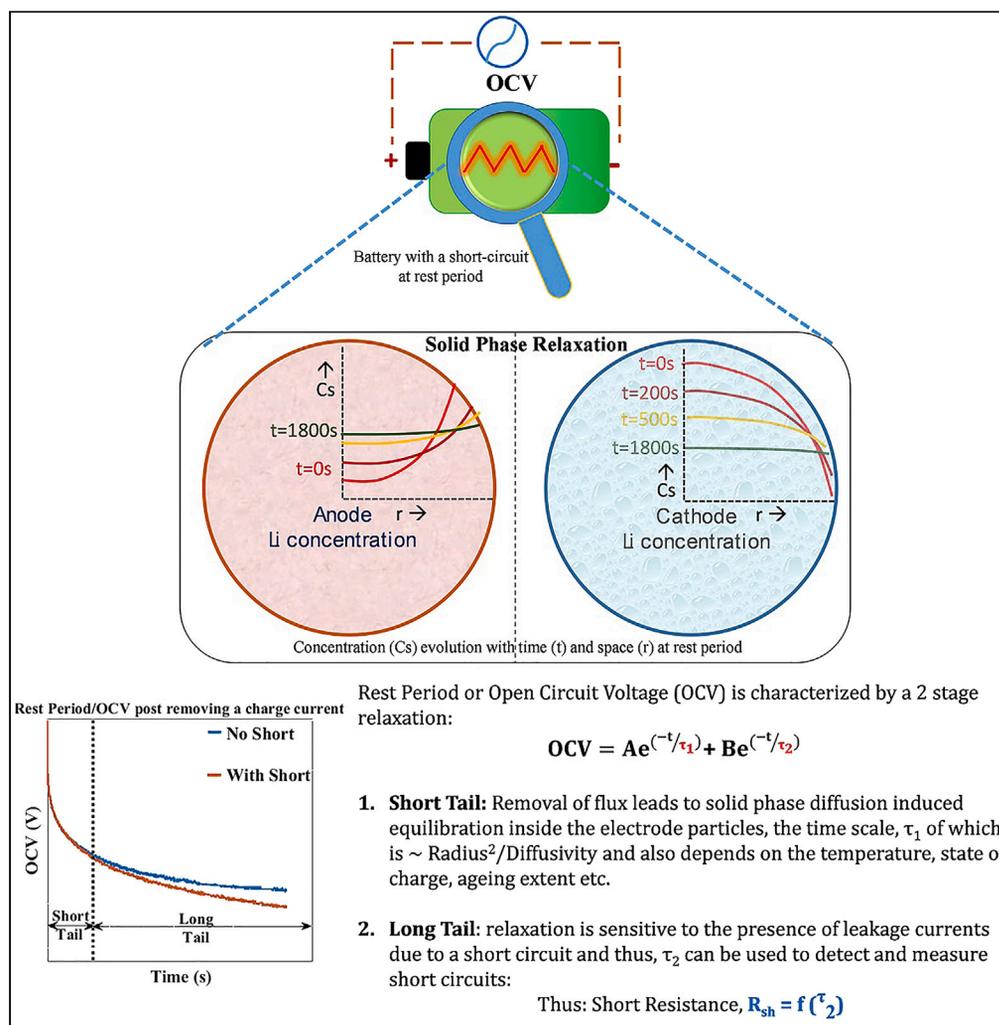Validated with experiments, the method is compatible for deployment onboard a device

Article

Isolation of relaxation times under open-circuit conditions: Toward prognosis of nascent short circuits in Li-ion batteries

Sagar Bharathraj,[1,3,*] Myeongjae Lee,[2] Shashishekar P. Adiga,[1,*] K. Subramanya Mayya,[1] and Jin-Ho Kim[2]

SUMMARY

Li-ion battery mishaps are primarily attributed to short circuits, which missed early detection. In this study, a method is introduced to address this issue by analyzing the voltage relaxation, after initiating a rest period. The voltage equilibration arising from solid-concentration profile relaxation is expressed by a double-exponential model, whose time constants, τ_1 & τ_2, capture the initial, rapid exponential contour and the long-term relaxation, respectively. By tracking τ_2, which is very sensitive to small leakage currents, it is possible to detect a short early on and estimate the short resistance. This method, validated with experiments on commercial batteries induced with short circuits of varying extents, has >90% prediction accuracy and enables clear differentiation between different short severities, while factoring in the influence of temperature, state of charge (SOC), state of health (SOH), and idle currents. The method is applicable across different battery chemistries and form factors, offering precise and robust nascent-stage short detection-estimation for on-device implementation.

INTRODUCTION

Lithium-ion batteries (LIBs) are ubiquitous in the modern-day world as they increasingly find applications in portable electronic devices, electric vehicles, and stationary storage. Attributes such as low self-discharge, thermal stability, high energy density, energy efficiency, and long life have paved way for them to be a top contender in the "green energy" pyramid.[1,2] As global economies commit to reduce their carbon footprint through steps like electrification, dependence on/adoption of energy sources like LIBs is set to rise significantly, both for stationary and mobile applications. However, occasional incidents of catastrophic failure due to thermal runaway and fires, particularly in large-format cells like that of a battery electric vehicle (EV/BEV), have unfortunately attracted skepticism regarding the safety of this technology.[3,4] One of the widely reported causes for such a failure is short circuits (SCs), whose early detection and monitoring on a battery management system (BMS) is crucial in preventing such mishaps.[5–7] While many SC detection protocols have been proposed in the literature, due to many of their handicaps like lack of early detection, dependence on huge, specific datasets, inaccuracy and difficulty in implementation, etc., they fail to meet the requirements for BMS deployment.[8,9] In this work, we attempt to solve these problems. At the core of the proposed approach lies the understanding that the LIB experiences a voltage recovery after charge/discharge current is interrupted, due to relaxation of concentration profiles developed inside solid electrode particles. The long-tail time constant of an open-circuit/rest-period voltage recovery profile is highly sensitive to the presence of leakage currents due to an overlap in their timescales. This presents a clear signal for very early detection of SCs and precise estimation of the short resistance. Validated with experiments on commercial batteries, we present a robust *in situ* protocol, toward early-stage short detection and accurate quantification (>90% precision) for device implementation, while needing minimal computational resources.

The paper has been divided into the following main sections: 1) in the present section, we lay the premise for this study by briefly giving an overview of the problem, with focus on how the present state-of-the-art algorithms lack on many important attributes, essential for device implementation. 2) Further, in the concepts section, a double-exponential (DE) model is derived from first principles, for expressing the spatio-temporal profile of a rest-period/open-circuit voltage (OCV), essential to the proposed short detection method. Further, we showcase how and why the DE-derived long-tail time constant, τ_2, of the rest period

[1]Next Gen Projects, SAIT-India, Samsung Semiconductor India Research SSIR- Bangalore, Bangalore, India

[2]Battery Material TU, SAIT, Samsung Electronics, Suwon, Republic of Korea

[3]Lead contact

*Correspondence:
s.bharathraj@samsung.com (S.B.),
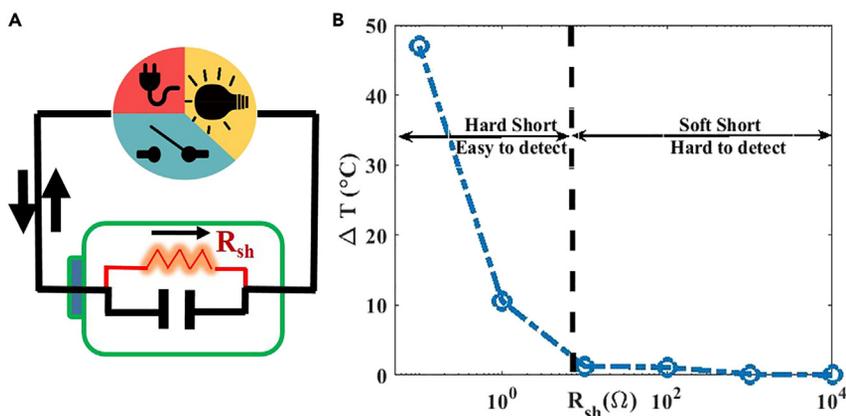shashi.adiga@samsung.com (S.P.A.)
https://doi.org/10.1016/j.isci.2023.106636

Figure 1. Battery short circuits and how they influence cell temperature

(A) Schematic of a battery induced with a SC of resistance, R_{sh}.

(B) The average temperature increase as a function of severity of short which is inversely proportional to the short resistance R_{sh}; The temperature profile is calculated using an electrochemical-thermal (ECT) model. Short detection strategies that rely on sensing temperature rise are not suitable for early-stage short detection (for example, $R_{sh} > 10\,\Omega$ for a mobile battery) as the average temperature increase is comparable to average temperature variations.

is sensitive to and can detect SCs and accurately estimate the short resistance, R_{sh}. 3) Later, in the methods section, the experiments performed as part of validating the proposed method are detailed. 4) In the results and discussion section, initially the results of the experimental validation are detailed. The effect of important variables like temperature, state of charge (SOC), and state of health (SOH) on the method and its predictions is explained. A summary of the evaluations performed is tabulated to showcase the robustness and accuracy of this method. We also discuss the applicability of this technique in real use case scenarios. 5) Furthermore, the underlying assumptions, pros-cons of this technique, pointers on how the method can be improved, and concluding statements are shared.

A SC is an unintentional electrical contact, established between the electrodes to form a closed electrical circuit, which is independent of an external load as shown in Figure 1A. The severity of the short is usually characterized by the resistance, R_{sh}, offered by the contact, with a lower resistance indicating a more severe short as it allows a higher current flow through the short. SCs are broadly of two types: internal SC (ISC)—where the electrical contact is inside the cell—and external SC (ESC)—where the contact is outside the cell. Based on the duration, the short can be a persistent one, where, once the short is initiated, it exists throughout the battery operation, unless intervened. The SC can also be an intermittent one, whereby phenomena like lithium dendrites exist only in certain operational windows (high currents/SOCs, low temperatures), often to get melted down due to self-heating and reformed several times.[10–12]

The establishment of a short is due to electrical, mechanical, or thermal abuses, either during the manufacturing stages (defects)[6] or during operation.[13] Once initiated, a short (ISC) usually goes through 3 main stages: initial stage; growth stage, and a final stage of thermal runaway. The initial stage is immediately after the establishment of an electrical contact between the electrodes, during which the ionic and electric current flow generates heat (Joule heating) but not enough to raise the cell temperature beyond normal operating temperatures[14]; this is also known as a soft-short stage. In the growth stage, due to heat accumulation, the cell temperature increases; consequently, ionic resistance decreases and these two mutually promote each other, causing a rapid increase in temperature; which is called a hard short. There have been attempts to put a threshold on the short resistance value for a hard-soft short transition. According to one industry standard (GB/T 31484-2015), the maximum leakage current allowed in a battery system to be classified as a soft short is C/3.7 (where C is the 1C current).[9,15,16] This translates to a short resistance, R_{sh}, of approximately 3Ω–6Ω for typical commercial mobile phone batteries (example: for a 4Ah battery with nominal voltage ~3.85V, $R_{sh} = [3.85V/(4A/3.7)] \sim 3\Omega$), with this number varying, depending on the battery capacity/form factor. An easier way to differentiate the soft-hard transition is the short resistance below which the signatures become noticeable. As shown in Figure 1B, the average temperature increase of the same 4Ah battery is calculated for different short resistances, R_{sh}, using an electrochemical-thermal (ECT) model (detailed in the upcoming methods section). The increase is visible below ~10Ω,

whereas, above 10Ω, there is hardly any noticeable change and should be ideally the zone in which the short detection should happen. If the soft short is allowed to progress through the hard-short stage, it causes breakdown of the electrolyte and an initiation of self-sustaining exothermic reactions causing a thermal runaway.[4] Thus, it is recommended that the short be detected in the soft-short/initial stage itself. Also, as the inception stage is usually long, unless the short is triggered by a sudden damage (in which case, the only option is to isolate the device), soft short presents an opportunity to get detected. However, as the short severity is low (high R_{sh}), its influence on the battery states is very subtle to be noticed, making reliable detection hard.[9,15] Not only do proposed methods in the literature not detect soft short but they also pose a few other concerns.

The prognosis and diagnosis related to SCs occur mainly in two ways. One, a long-term approach, where the SC formation itself is prevented and two, an on-device algorithmic approach, where once the short is formed, it is detected as early as possible. In the first approach, the focus is given at the cell design stage with attention on material choices, to increase thermal stability of cells, for example, solid-state batteries,[17] eliminating flammable organic electrolytes, and/or at a preventive level with an in-built fail-safe mechanism[18,19] that arrests catastrophic failure. It can also be in terms of avoiding operational windows known to induce shorting like shrinking the SOC range of operation. The second approach is that of an onboard algorithm to detect SCs, which normally happens via noticing a deviation or anomaly in an observed battery state with reference to that of a healthy cell whereby breaching a threshold value is flagged as a fault. Usually the states monitored are cell temperature, voltage, capacity, and properties like internal resistance[20–23] or an index which is basically a weighted combination of these different states, as used by recent machine learning/data driven-based techniques.[24,25] Different observers, such as extended Kalman filter (EKF),[26–28] Luenberger observer,[29] etc. have been used to detect SCs. Recently, a pulse current-based technique was shown to work excellently in detecting soft short, as soft as 200Ω.[9] However, this method requires high-amplitude currents that may not be allowed by the power management integrated circuit (PMIC) onboard different battery applications, apart from the fact that an onboard ECT model was also necessary to monitor the states and accordingly calculate the pulse current required. However, apart from the practicality aspect of these algorithms, one of the major handicaps is their insensitivity toward detecting early-stage SCs, which is ideally when they should be detected. This is due to the observation that the sensitivity of the battery signatures, typically used in detecting SCs, when the short severity is very low (soft short) is very questionable. Previously proposed short detection signatures include temperature increase (as shown in Figure 1), heat accumulation, voltage/capacity/internal resistance change, etc.[9] However as shown in Figure 1 and through experiments in our recent work,[30] which proposes a new metric for SC quantification and also discusses many of the available methods along with its handicaps, these features hardly show any variation between a healthy cell and a cell with a soft short (>50Ω). Thus, they fail in detecting early-stage SCs. In addition to these typically used short detection signatures, conventional methods such as self-discharge as a measure of SC severity are not appropriate for onboard applications as they take a long time for measurement. Thus, these proposed techniques suffer from one or more of the problems including: 1) inability to detect early-stage short, 2) requirement for long-term data accumulation, 3) inaccuracy, 4) lack of sensitivity, whereby even though the short may be detected, however is not sensitive enough to differentiate between the different short severities, 5) lack of specificity whereby the features used need not be specific to short (e.g., capacity reduction can also be due to degradation[9]), 6) lack of adaptability across different battery chemistries and form factors, and 7) requiring heavy computational resources. In this study, we attempt to address all these issues with a compelling solution.

The voltage relaxation during a rest period or open-circuit conditions is attributed to the equilibration of the gradients in the concentration of lithium inside the electrode particles. This relaxation is seen to evolve in two stages, a sudden exponential decay/rise (after removing a charge/discharge current) and a long-term saturation. A DE model is proposed to capture this behavior. From first principles, expression for the spatiotemporal variation of voltage is derived under rest and low c-rate conditions. Characterized by two exponentials, the time constants (τ_1, τ_2) represent the two distinct stages of the voltage evolution. It is observed that the time constant associated with the long-term saturation (τ_2) is influenced by the slightest of leakage currents, due to their overlapping time scales. By monitoring this time constant, early detection and precise estimation of SCs, as soft as 500Ω (considering mobile phone batteries), are possible with very high sensitivity and robustness. The method is not restricted to just rest-period conditions, as long as the (dis)charge current is within a threshold limit to allow the timescale overlap. Additionally, the method has been validated with experiments on commercial mobile phone batteries, induced with a short in the

range of 50Ω–500Ω. Influence of factors like temperature, SOC, SOH, and c-rates was accounted, to reveal very encouraging prediction accuracies (>90%) and robustness. The method can be tailored across battery chemistries and form factors (single/multi-cells, packs). The novelty of the work presented here lies in the fact that there is no requirement of additional hardware or onboard electrochemical model or extensive data collection required for short detection like in earlier works. The protocol also exhibits essential attributes of in-operando early detection, sensitivity, precision, and minimal computational requirements, which are the need of the hour for device-implementable fault-detection algorithms.

Concepts

A DE model for rest-period voltage

The terminal voltage, V, of a battery can be expressed[2] as shown in Equation 1 below:

$$V = OCV + IR = OCV \ (at \ rest \ period \ when \ I = 0) \qquad \text{(Equation 1)}$$

Where OCV is the open-circuit voltage of the battery, I is the current, and R is the resistance of the battery. The OCV of the battery is given by the difference in OCPs (open-circuit potentials) of the cathode, U_p, and the anode, U_n. Equation 1 can be differentiated with respect to time to get time variation of the OCV as follows:

$$\frac{dV}{dt} = \frac{dOCV}{dt} = \frac{d\ (U_p - U_n)}{dt} = \frac{dU_p}{dt} - \frac{dU_n}{dt} \qquad \text{(Equation 2)}$$

In the rest period, the relaxation is attributed to the solid-phase diffusion-induced equilibration of lithium ion concentration inside the electrode active material particles.[31] Thus, the change in the particle surface concentration (Cs) and the resultant voltage variation in time is due to the variation in the concentration (or SOC). Accordingly, we modify Equation 2 as follows:

$$\frac{dU_p}{dt} - \frac{dU_n}{dt} = \frac{\partial U_p}{\partial SOC_p}\frac{\partial SOC_p}{\partial t} - \frac{\partial U_n}{\partial SOC_n}\frac{\partial SOC_n}{\partial t} = \frac{\partial U_p}{\partial SOC_p}\frac{1}{Cs_{pmax}}\frac{\partial Cs_p}{\partial t} - \frac{\partial U_n}{\partial SOC_n}\frac{1}{Cs_{nmax}}\frac{\partial Cs_n}{\partial t}$$

$$\text{(Equation 3)}$$

Where, SOC_n and SOC_p are the SOC of the anode and cathode, respectively, which is the ratio of the lithium ion concentration at the solid particle surface (Cs_n,Cs_p) to the concentration corresponding to the maximum theoretical capacity of the respective electrode ($Cs_{n,max}$, $Cs_{p,max}$). The derivative of the OCV with SOC is known for a particular electrode and is usually a polynomial expression, which can be absorbed into the solution later. Also we assume that the temperature variation is negligible during this time period. To proceed further, we consider the spherical diffusion equation with the boundary and initial conditions (BCs, ICs) as shown in Equations 4 and 5, respectively

$$\frac{\partial Cs}{\partial t} = \left(\frac{1}{r^2}\right)D\left[\frac{\partial}{\partial r}\left(r^2\frac{\partial Cs}{\partial r}\right)\right] \qquad \text{(Equation 4)}$$

$$BC = \frac{\partial Cs}{\partial r}\Big|_{t \geq 0} = 0 \ @ \ r = 0 \ \& \ r = R \ \& \ IC = \frac{\partial Cs}{\partial t}\Big|_{r = R} = Csi \ @ \ t = 0 \qquad \text{(Equation 5)}$$

Where D is the diffusivity, r is the radial position with R as the radius of the particle, and Cs_i is the concentration at the surface of the particle at the beginning of the rest period. With homogeneous boundary conditions (flux being 0 at both the center and surface), variable separable solutions are applicable, whereby the spatial and temporal domain solutions can be separated. This is only valid for rest conditions as the boundary conditions shown in Equation 5 become homogeneous. Otherwise, $\frac{dCs}{dr}$ = intercalation flux (J) (at r = R) is non-zero during non-rest conditions and Equation 6 stands invalid. To proceed further, we scale the concentration by the initial concentration ($C_{s,i}$), at the beginning of the rest period, time by the diffusion timescale i.e. $\tau = R^2/D$, and radial dimension by the radius, R, i.e.,

$$C_s^* = \frac{C_s}{C_{s,i}}; r^* = \frac{r}{R}; t^* = \frac{t}{\tau} = \frac{t}{R^2/D} \ ; \qquad \text{(Equation 6)}$$

Using the above scaling i.e. Equation 6 in 5 gives

$$\frac{\partial Cs^*}{\partial t^*} = \left(\frac{1}{r^{*2}}\right)\left[\frac{\partial}{\partial r^*}\left(r^{*2}\frac{\partial Cs^*}{\partial r^*}\right)\right] \qquad \text{(Equation 7)}$$

The boundary conditions accordingly get modified as

$$BC = \frac{\partial Cs^*}{\partial r^*}\Big|_{t \geq 0} = 0 \text{ @ } r^* = 0 \text{ \& } r^* = 1 \text{ \& } IC = \frac{\partial Cs^*}{\partial t^*}\Big|_{r^* = 1} = 1 \text{ @ } t^* = 0 \qquad \text{(Equation 8)}$$

Variable separable form is applicable for the above equation, as shown below:

$$Cs^*(r^*, t^*) = M(r^*) \times N(t^*) \qquad \text{(Equation 9)}$$

Equation 9 in Equation 7, separating the spatial and temporal parts and equating them to a constant implies:

$$\left(\frac{1}{N}\right)\frac{\partial N}{\partial t^*} = \left(\frac{1}{M}\right)\left(\frac{1}{r^{*2}}\right)\left[\frac{\partial}{\partial r^*}\left(r^{*2}\frac{\partial M}{\partial r^*}\right)\right] = -\gamma^2 \qquad \text{(Equation 10)}$$

The spatial part can be simplified to

$$r^{*2}\frac{\partial^2 M}{\partial r^{*2}} + 2r^*\frac{\partial M}{\partial r^*} + \gamma^2 r^{*2} M = 0 \qquad \text{(Equation 11)}$$

The above equation is solved to get

$$M(r^*) = \frac{A \, Sin(\gamma r^*)}{r^*} + \frac{B \, Cos(\gamma r^*)}{r^*} \qquad \text{(Equation 12)}$$

Here A and B are constants to be determined from the boundary conditions. From the symmetry boundary condition, it is clear that B has to be equal to zero. The constant γ is determined from the boundary condition r* = 1. Therefore, the eigenvalue γ assumes discrete values or $\gamma_n = n\pi$, where n is an integer. Similarly for the temporal part, the solution would be

$$\left(\frac{1}{N}\right)\frac{\partial N}{\partial t^*} = -n^2\pi^2 \qquad \text{(Equation 13)}$$

This is solved to get

$$N(t^*) = e^{-\gamma_n^2 t^*} = e^{-(n^2\pi^2 t^*)} \qquad \text{(Equation 14)}$$

Combining the solutions in Equations 12 and 14, we get

$$Cs^*(r^*, t^*) = \sum_{n=1}^{\infty} \left(\frac{A_n}{r^*}\right)e^{-(n^2\pi^2 t^*)} Sin(n\pi r^*) \qquad \text{(Equation 15)}$$

Where n is an integer representing the harmonics of the overlapping modes and τ is the time constant of the particular harmonic. As seen, the concentration profile has an exponential profile in the temporal domain, indicating a decay, relaxation, and a sinusoidal profile in the spatial domain with overlapping modes. Although the equation describes the full solution using harmonics extending until ∞, for all practical purposes, 2 harmonics are good enough to capture the state field (concentration in this case). Also, Equation 15 is a solution for both the electrodes, with their respective boundary and initial conditions. As Equation 15 solves only the time derivative of concentration in Equation 3, we need to solve for the time derivate of the voltage. By integrating the temporal solution part of Equation 15, for both the anode and cathode, and also keeping the harmonics to n = 2, we get the expression for the voltage profile as shown below:

$$V = K_1(n, R)e^{-\left(\frac{t}{\tau_1}\right)} - K_2(n, R)e^{-\left(\frac{t}{\tau_2}\right)} \qquad \text{(Equation 16)}$$

Although the time constant, τ, of both the anode and cathode should be present in the equation above, the limiting electrode τ (in our case, the cathode) is what matters in this case. This is shown in Figure S1 of the supplementary information, where the cell voltage time constants as compared to that of the potential of the individual electrodes, for rest periods initiated at various SOCs, are shown. The results, which were generated using simulations (detailed in the next sub-section) with parameters as those of the battery used in this study (detailed in the methods section), show that the cell voltage time constants almost always follow those of the cathode as it is the limiting electrode due to a larger radii and thus a larger diffusion timescale. The coefficients (K_1, K_2) can be solved by using the boundary conditions and the orthogonality relations for the basis functions (sin (nπr*)/r, but our main intent here is to capture the surface concentration (at r = R), and thus the voltage to show that the voltage profile in the temporal domain, during a rest period, can be expressed by a combination of two exponentials. This, as we will see soon, essentially captures the short
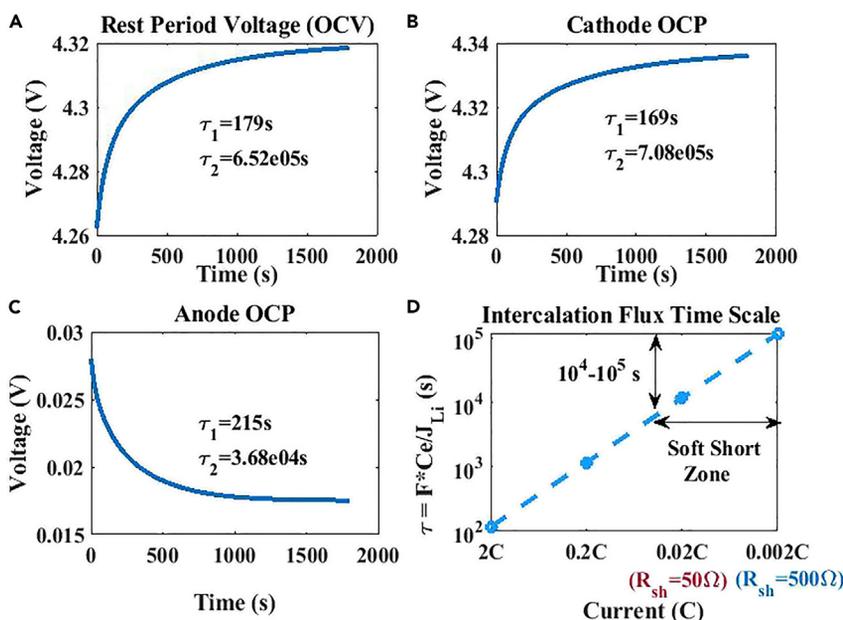
Figure 2. How and why short circuits influence rest-period voltage relaxation time constant τ_2
Rest-period voltage relaxation profiles generated using P2D simulations, after removing a discharge current at 90% cell SOC, for the (A) cell, (B) cathode, & (C) anode with the values of the time constants τ_1 & τ_2 indicated in the inset; (D) the dependence of intercalation flux time scales on the c-rate. The c-rates corresponding to leakage current through the short circuits with R_{sh} values of 50 and 500 are indicated for guidance.

tail of decay/rise and a long tail of relaxation of the rest-period voltage profile, with τ_1 & τ_2 being the associated time constants, respectively. The different electrochemical phenomena contributing to these two stages of the OCV profile include an ohmic resistance-induced sudden voltage drop/rise, battery's double-layer capacitance, charge transfer resistance contributions, and most importantly a gradient-induced Li diffusion inside the electrode particles, considered to be the rate-determining step for Li-ion batteries.[32] There are parameters like SOH, SOC, and temperature that will influence the voltage profile,[31] and thus, it is necessary to study the influence of the same on the time constants. First, however, our hypothesis that SCs influence the long-tail relaxation time constant i.e. τ_2 needs to be established.

SCs & long-term relaxation: R_{sh} & τ_2

A typical rest-period voltage profile, after removing a discharge current of 0.2C at 90% cell SOC and room temperature (298K), is shown in Figure 2A. This was generated using a pseudo 2-dimensional (P2D) ECT model.[33] The code was written in MATLAB, and the simulations were run on an Intel (R) Core (TM) i7-6700HQ CPU @ 2.6 GHz, 8 GB RAM. The P2D parameters corresponded to those of an NG (natural graphite)-LCO (lithium cobalt oxide) battery of 4Ah capacity (tagged battery 3 in our study and to be detailed in the next section), whose electrochemical parameters are available in our previous studies.[9,34] The voltage profile can be segregated into individual contributions from both the electrodes as shown through Equation 2 and now in Figures 2B and 2C. The time constants of these profiles are shown as well. The short-tail time constant, τ_1, is of the order of 10^2s. For an electrode particle with a radius in the order of μm and diffusivity in the range of 10^{12}-10^{14} m^2/s (at 298K), the ionic-diffusivity timescale τ is ~R^2/D, which in this case would be ~10^2s and is thus consistent with the τ_1 for the electrodes. The long-tail time constant, τ_2, is in the order of 10^5s, which will go to ∞s, for higher harmonics (n > 3) of the voltage equilibration. Also, we see that the cell voltage time constants follow those of the cathode potential as it is the limiting electrode due to a higher diffusion timescale as explained earlier. Now, the correlation of the time constants with that of a short-linked leakage current is of interest.

In the case of a short, the leakage current is of the order of V_{cell}/R_{sh}, where V_{cell} is the cell voltage. For a short of 50 Ω at a V_{cell} of ~ 4V, this corresponds to 0.08A current (0.02C for a 4Ah battery). Thus, a 50Ω short corresponds to a 0.02C discharge, to be sustained through the short. Now, the intercalation process has a timescale, which is of the order of $(FC_e)/_{|J_{Li}|}$,[35] where F is the Faraday's constant in As/mol, Ce is the molar

concentration of lithium in the electrolyte phase (mol/m^3), and J_{Li} is the intercalation current density in A/m^3. For different c-rates, this variation is shown in Figure 2D. As seen, typical current rates (>0.2C) have a timescale in the range of 10^2-10^3 s, whereas a soft short in the range of 50Ω–500Ω (which corresponds to 0.02C–0.002C current) has a τ in the range of 10^4-10^5 s, which matches the voltage long-tail relaxation time constant, τ_2. This is because an SC is equivalent to a low c-rate discharge for the battery, whose magnitude depends on the short severity and voltage. This leakage current leads to electrochemical reaction that alters the lithium utilization levels in the electrodes. This in turn changes the voltage relaxation profile, which otherwise would have been only due to Li concentration profile relaxation inside electrode particles, especially the long-term, when the short severity is low. However, if the leakage currents were in the range of 0.2C and above (which is the case for $R_{sh} \leq 10\Omega$), its timescale would overlap with that of τ_1. However, our intention is to detect a short in its early stages ($R_{sh} \geq 50\Omega$). Thus, the overlap of timescales (between a short-induced leakage current and voltage relaxation time constant, τ_2) helps in detecting, amplifying, and quantifying the effect of a short, by isolating the timescales of a rest-period voltage profile. Due to the leakage current, it is appropriate to term the voltage relaxation as voltage decay. Thus, by isolating and measuring the long-term voltage relaxation/decay time constant, τ_2, and its decrease, a short can be detected and its magnitude R_{sh} can be estimated.

Methods: Experiments; ESC as an emulation of ISC

To validate our hypothesis that the long-tail time constant decrease is an indicator of the presence of an SC and the magnitude of decrease, the severity of the short, R_{sh}, we conducted experiments on commercial batteries, which were subjected to shorting. Inducing ISC in a controlled manner to monitor battery states is difficult as the causative factors are varied and random, presenting significant experimental implementation challenges. Although abusive loading tests (compression, indentation, penetration, bending)[18,36–38] mimicking the real-world scenarios are available, these are to characterize the mechanical integrity and thermal stability of the batteries. In addition, these are *ex situ* approaches toward offline risk evaluation and not for onboard implementation. This is where ESC helps. As far as ESC & ISC are concerned, the main difference is in the position of the short (external vs. internal), thus the joule heat source and self-heating magnitude (more for ISC). However, in the initial stages of the SC, both ESC & ISC have very similar effects on the battery states. Also, ESCs offer a huge advantage due to the fact that the short resistance is measurable and controllable, and the experiments are repeatable to generate quantitative relationships between the battery states and the short severity. This has been a popular way of studying SCs.[9,15,24] Thus, to emulate shorting, we connect an external short in the form of a rheostat/shunt resistance across the battery terminals, whose resistance can be changed as per the requirement.

For the experiments, we chose a commercial NG-LCO mobile phone battery, tagged battery 1, with a rated capacity of 1.85Ah. For certain specific validation cases, a few other batteries of the same chemistry, tagged as battery 2 (4.85Ah) & battery 3 (4Ah) were used. The electrode OCPs and its temperature derivatives of these batteries are given in Figure S2 of the supplementary information. These batteries have maximum/nominal/minimum voltages of 4.45V/3.85V/2.75V, respectively. As mentioned earlier, their ECT parameters are available in our previous studies.[9,34] In the experiments, the battery is connected to an external shunt (R_{sh} = 50Ω-100Ω-200Ω–500Ω) and without a shunt (∞ Ω). Battery 1 was subject to long-term cycling under the popular constant current-constant voltage (CC-CV) charge, CC discharge protocol, where rest periods of half an hour duration were imposed after a full charge and discharge. The current profile used and the resultant battery voltage profile are shown in Figure S3 of the supplementary information. Ambient temperatures, T, of 18°C, 23°C, & 32°C were used. Thus, around 15 units of battery 1 (5 short resistances including ∞Ω and 3 temperatures) were subjected to cycling, generating around 300 cycles of charge-discharge-rest period data for one R_{sh}-T pair. Rest period data were generated at different conditions for the other batteries (battery 2 & 3), depending on the analysis performed; which will be detailed as and when they are presented. These rest period data, generated for different battery sets under varied conditions, were subjected to the analysis using the DE model. Further, the time constants (τ_1 & τ_2) were extracted, to see if τ_2 is a dependable feature for an early short detection and accurate R_{sh} estimation, which will be discussed next.

RESULTS AND DISCUSSION

Proof of Concept: SC diagnosis with time constant τ_2

The rest period profile of battery 1, after 50 cycles of charge-discharge, after a CC-CV charge until 4.47V at 32°C, for different short resistances R_{sh} is as shown in Figure 3A. The 2-staged voltage relaxation is evident, with the ∞Ω case clearly showing a tendency to saturate, whereas, there is a decay for the batteries
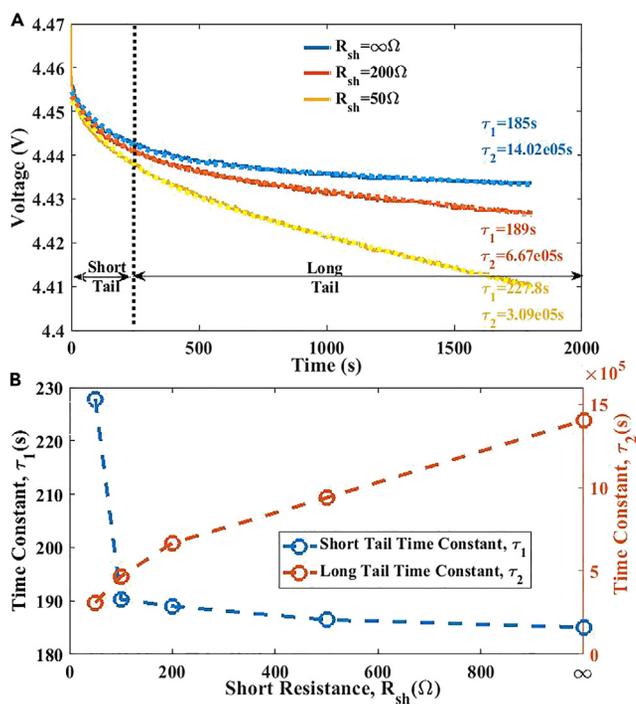
Figure 3. Proof of Concept with visualization on experimental data
(A) Variation of Rest-Period Voltage with time for different values of short resistance, R_{sh}, at 32°C with the DE model fit and corresponding time constant values of τ_1 & τ_2. (B) Variation of time constants τ_1 & τ_2 with short resistance, R_{sh}.

connected to a short of 200Ω and 50Ω, due to the persistent short-induced leakage current. The voltage profiles, fit to the DE model, are shown in Figure 3A. The profile fit has an R^2 value >0.99, proving to be an excellent fit, hardly recognizable from the actual data and a validation of our proposed model. The short- and long-term time constants i.e. τ_1 & τ_2, respectively, are given for all the 3 curves in Figure 3A and plotted separately as a function of the short resistance, R_{sh}, in Figure 3B. An essential attribute of an effective short detection feature is the ease with which it is able to detect early-stage SCs ($R_{sh} \geq$ 50Ω) and the sensitivity with which it can differentiate between SCs of different magnitudes. The consistent decrease in τ_2 with a decrease in R_{sh}/increase in short severity is clearly seen in Figure 3B, making it a strong and a sensitive metric to detect SCs. SCs, which are as soft as 500Ω show a 30% decrease in τ_2 as compared to the no-short/∞Ω case, whereas for a 50Ω short, the τ_2 is almost $1/3^{rd}$ of the no-short case. This is a significant decrease and thus easy to differentiate between different short severities that too in the soft-short zone, which is otherwise very difficult to differentiate from each other. Whereas τ_1 seems to be almost uninfluenced by the short resistance especially for $R_{sh} > 100$Ω but increases suddenly at low short resistances as seen here and as shown in Figure S4 of the supplementary information, where the same plot is shown for another ambient temperature, T = 18°C. The influence of $R_{sh} \leq 50$Ω on τ_1 is due to the overlap of timescales associated with the leakage currents in this short regime and typical τ_1 values as discussed earlier for Figure 2D. Thus, for a soft-short regime, in the range of $R_{sh} > 50$Ω, τ_2 is a relevant and sensitive feature and an appropriate parameter for early short detection and estimation. Although the post-charge rest period is analyzed in this study, similar inferences will be applicable for a post-discharge rest period. However, a post-charge rest period is more practical as far as data availability is concerned.

As rest-period relaxation predominantly involves solid-phase diffusion-induced equilibrium, any parameter that influences the diffusivity and its timescales (like T, SOC, and radius of the particle (R) etc.) would influence the rest-period voltage as well. In fact, galvanostatic intermittent titration technique (GITT) where diffusivity coefficients are estimated at various SOCs, and temperatures through long rest periods,[39] is based on this knowledge. Thus, to check the robustness of the proposed method, understanding the influence of conditions (T, SOC, and SOH) on the rest period/OCV profile[31,40] and thus the time constant, τ_2, is very important.
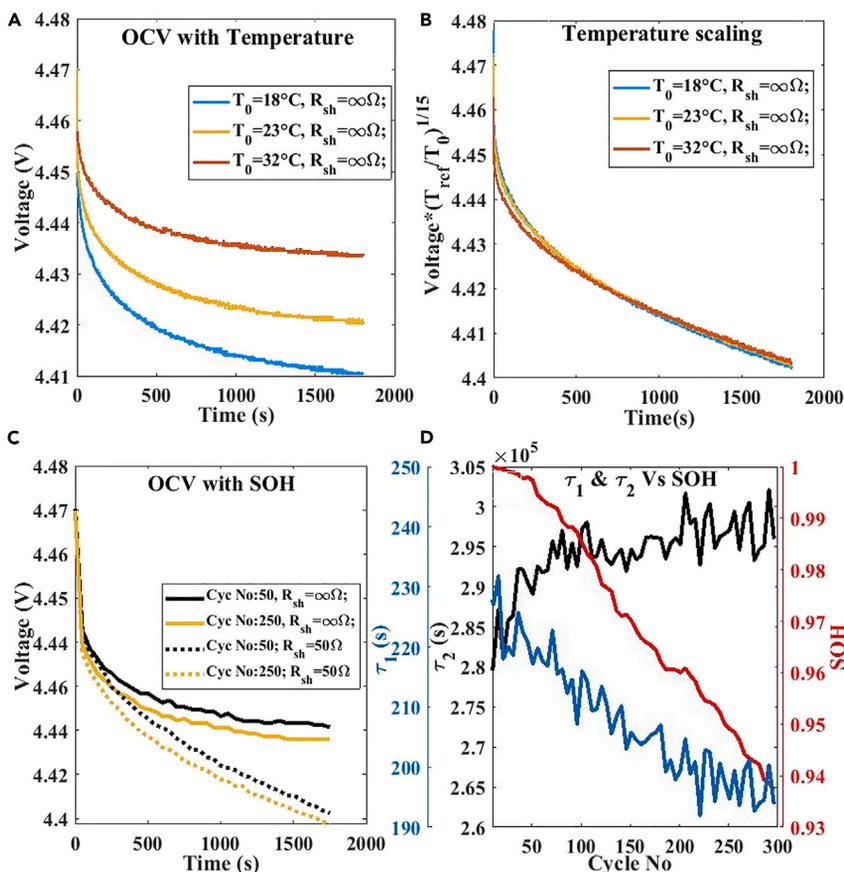
Figure 4. Influence of temperature & aging/SOH

Variation of Rest-Period/Open-Circuit Voltage profiles with time (s) at (a) different temperatures (b) and its scaling. (c) Variation of Rest-Period/Open-Circuit Voltage profiles with time at different cycle numbers and short resistance, R_{sh}, with the (d) variation of the time constants τ_1 & τ_2 and State of health, SOH, with cycle number.

Influence of parameters: Temperature, SOH, & SOC

A very important variable, whose influence on τ_2 and subsequently τ_2's utility in detecting SCs and estimating the short resistance, R_{sh}, needs to be analyzed, is the ambient temperature, T. The rest-period voltage profile for battery 1 for different ambient temperatures and short resistance is as shown below in Figure 4A. The voltage drop seems to be significantly high at lower temperatures, which is intuitive, due to the diminished transport properties at lower temperatures. As the thermal energy of Li is directly proportional to the temperature, T, the temperature dependence of diffusivity can be expressed via the Arrhenius equation.[41] The voltage scaling with temperature, especially in the rest period, can be understood by the variation of the OCP (open-circuit potential) of the individual electrodes with temperature as shown in Figure S2 of the supplementary information. From the same, an empirical relationship can be drawn, to scale the voltage with temperature as shown in Figure 4B. Once this scaling is done, the voltage data can be processed as usual by fitting them to the DE model, to extract the time constants for further analysis. This eliminates the sensitivity of extracted τ_2 on the operational temperature.

It is understood that batteries age with use. The process of charge and discharge over cycles inevitably induces parasitic side reactions at certain voltage and current windows, leading to deterioration of battery performance with time. Battery degradation or aging is caused by different phenomena,[12,40,42] leading to loss of lithium inventory (LLI), loss of active material (LAM), etc.[2] This eventually manifests as an increase in battery resistance and capacity loss,[43,44] which in turn will influence the rest-period voltage profile as well. Thus, it is of interest to see how battery degradation will influence the τ_2 profile with time and short resistance R_{sh}. The extent of aging is usually measured by a popular metric called the SOH, which is the ratio of the available cell capacity (typically the discharge capacity) to the rated capacity of the battery,

under the same reference conditions.[45,46] The capacity is usually measured by coulomb counting, which measures the amount of current injected/drawn from the battery during charge/discharge. In our study, we utilize the same concept and SOH is calculated as the ratio of the full discharge capacity to the rated capacity of the battery, which is 1.85Ah in the case of battery 1. The rest-period profile after the CV phase of charging is shown in Figure 4C for different short resistances with cycle numbers at 32°C.

As seen, irrespective of the value, given a short resistance, the rest-period voltage profile is influenced by the battery aging. At first sight, it looks like the initial few seconds (<300s) seems to be affected by aging. The long tail, which seems more or less parallel to the 50th cycle profile, seems to be unaffected by aging, for both the no-short and 50Ω case. But this can be confirmed only by looking at the variation of the time constants with cycle number. As seen in Figure 4D, for a 50Ω short case, the SOH decreases to ∼94.5% at the end of 250 cycles, and we also see how the τ_1 & τ_2 values vary with cycle number. As confirmed from the visual inspection in Figure 4C, τ_1, the initial-stage time constant, decreases with cycle number/SOH (230s–190s, a drop of 18%). Whereas τ_2, which is the time constant for the long tail, almost always remains a constant as expected (with a mean around 2.95×10^5s, which is what is seen in Figure 3B for battery 1 at $R_{sh} = 50\Omega$), except for the initial few cycles. This can be ignored as batteries do take a few cycles to settle (due to SEI [solid-electrolyte interphase] formation,[2] capacity recalibration, etc.)

It may seem as if the variation of τ_1 is correlated with the SOH as they both decrease with cycle number; however, as seen in the Figures S5 of the supplementary information, which shows the variation of τ_1 & τ_2 vs. SOH for other conditions, this is not the case. For example, as seen with R_{sh} = 100Ω & 500Ω, for 32°C in Figure S5, τ_1 remains almost a constant with cycle no/aging. But, the non-influence of SOH on τ_2 can also be seen as shown in the same, thus making a case for τ_2 to be a metric, specific to long-term system relaxation that can only be influenced by leakage currents due to phenomena like an SC. In addition, the slight and random variations in τ_2 with cycle number hardly influence the short resistance, R_{sh}, estimation, as we will see in a later section. It is to be noted that these observations have been made for cycle numbers <300 or an SOH >85%, whichever is earlier, as below 85% SOH non-linear effects like sudden death come into the picture.[45] Although low SOH cases can be addressed as well with the proposed method, this is not given much attention, as batteries are usually discarded when their SOH drops below 80%.[44,47]

The rest-period profile and thus the time constant, τ_2, is influenced by the SOC too as the solid-phase diffusivity depends on the concentration of lithium in the electrode particles or the SOC.[41] The rest-period profiles were triggered at various different SOCs for a healthy ($R_{sh} = \infty\Omega$) battery 3, while performing GITT, and the profile is as shown in Figure 5A. For a better visual experience, the reduced voltage (voltage – initial voltage at t = 0s/beginning of rest period) profile is plotted. The time constant, τ_2, for these profiles, as a function of the SOC (SOC at which the rest period is triggered) is shown in Figure 5B. As is evident, the influence is quite significant with τ_2 decreasing with SOC, indicating that the system needs more time for equilibration. This can be explained by the understanding that, as charging continues to fill up/lithiate the anode particles, the resistance also increases due to lack of vacant sites in the particles, leading to slower rate of equilibration. We do not have much data on the influence of SOC on τ_2 of short-induced cells except for the one shown in Figure S6A of the supplementary information, where rest-period profiles induced at two different voltage points of 4.43V (95% SOC) & 4.35V (85% SOC) are shown for battery 1. This is due to the reason that the SC is detected based on the deviation from the healthy cell time constant, τ_2, and the short resistance, R_{sh}, is estimated based on the magnitude of the deviation, as we shall see soon.

We also took a look at how batteries of a similar chemistry (NG-LCO in this case) but with a different active material loading (capacity) would behave under the lens of the present study. The rest-period voltage data generated after a CC-CV charging with the CV voltage set at their respective prescribed limits for the 3 types of batteries (1, 2, & 3) are shown in Figure S7A, and the variation of τ_2 with R_{sh} is shown in Figure S7B. Just like in Figure 3C, where τ_2 vs. R_{sh} was plotted for battery 1, we see a similar profile for batteries 2 & 3 in Figure S7B. The batteries may have different τ_2 values for the same short resistance, R_{sh}; however, the trends are very similar and values also are quite close to each other. The different values of τ_2 can be attributed to the fact that the electrode geometry (loading, porosity, radius) is different for these batteries and the CV limit, after which the relaxation was initiated, is also different, leading to different SOC values (whose influence on τ_2 we just discussed) at which the relaxation has been induced. In any case, when it comes to estimating the short resistance, R_{sh}, the magnitude of the decrease in τ_2 relative to that of the
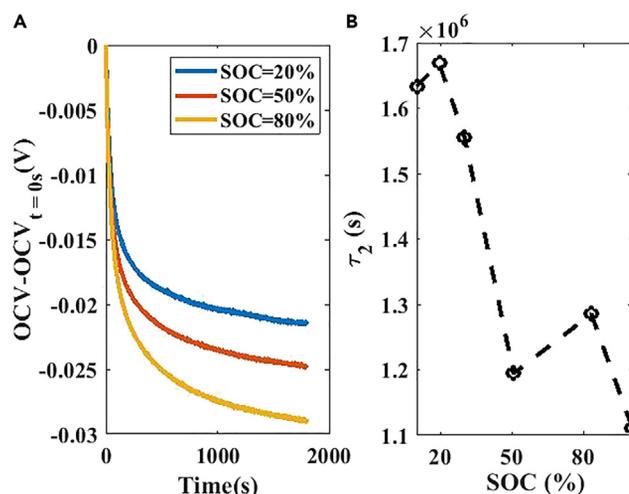
Figure 5. Influence of SOC
Variation of (A) Rest-Period/Open-Circuit Voltage (reduced voltage) with time at different SOCs and the (B) time constant τ_2 with SOC for the same.

τ_2 at no short or $\Delta\tau_2 = \tau_{2,Rsh} - \tau_{2,Rsh=\infty\Omega}|$ is what is required as discussed earlier and will be elaborated later in section R_{sh} estimation with τ_2.

Application during idle periods/low c-rate and the threshold limit

Although the method has been proposed with rest-period data, it may be difficult to collect the same in practice. Devices like mobile phones are almost always in use (discharged) or are charged or both. Even when software updates are installed, the device is switched off only for a few minutes with the PMIC always running on low power/current. Thus, an actual rest period, that too for a duration of 30 min, is highly unlikely on such devices whereas, for applications like electric vehicles (EVs) and laptops, rest-period data can still be collected when they are not in use/switched off. In any case, the question would be if this method is applicable when the current is $\neq 0$ and if yes, the maximum current/c-rate until which it is valid.

To answer this question, we refer back to Figure 2D, where we established the whole premise of this work, which is based on the overlap of the timescales of leakage currents associated with soft short and the relaxation time constant, τ_2. Therefore, as long as the voltage drawn is for current rates, whose timescale is in the range of $\tau > 10^4$s (so as to overlap with the timescales of leakage currents of a short of resistance, $R_{sh} \geq 50~\Omega$), one should be able to deploy this method. To test this, we collect the voltage data at low values of c-rate for different short resistances, R_{sh}, and see if the trend of τ_2 vs. R_{sh} is decipherable as that for the rest period. To mimic a real-world scenario as closely as possible, battery 3 (detailed in the methods section) was discharged from 4.3V at C/8 (assuming a very heavy usage of the battery by running power-hungry applications like gaming, etc.) for 30 min and then at a very low c-rate of C/20 for a period of 30 min. C/20 would be a realistic use case scenario as a full battery charge typically lasts for 20 h, whereas during idle periods (device kept on overnight), the discharge rate would be < C/50. The c-rate segregated rest period voltage profile is shown in Figures 6A and 6C for C/20 and C/8, respectively. The initial jump in the C/20 voltage profile is due to the sudden removal of the C/8 discharge current and a shift to C/20. The time constant, τ_2, for these two c-rates for different short resistances, R_{sh}, is as shown in Figure 6B.

As seen, the trend in the time constant τ_2 with short resistance R_{sh} is clear for C/20 with the profile being very similar to that of the rest-period case (Figure S7B of the supplementary information, related to Figure 6), whereas there is no trend for C/8. This is due to the requirement of timescale overlap, whereby, for C/20 (0.05C), it is very close to the range necessary for overlap with $R_{sh} \geq 50\Omega$ (0.02C) and it is not for C/8 (0.125C). This proves our observation that the c-rate limit to which this method is valid is determined by the short severity range to be detected. For example, in our study, as the objective is to detect early-stage short or $R_{sh} \geq 50\Omega$, the c-rate limit of operation should be $\sim$0.02C (or lower) to enable the timescale overlap. Whereas for voltage profiles extracted for higher c-rates (>0.1C), only harder SCs ($R_{sh} \leq 10\Omega$) can be detected.
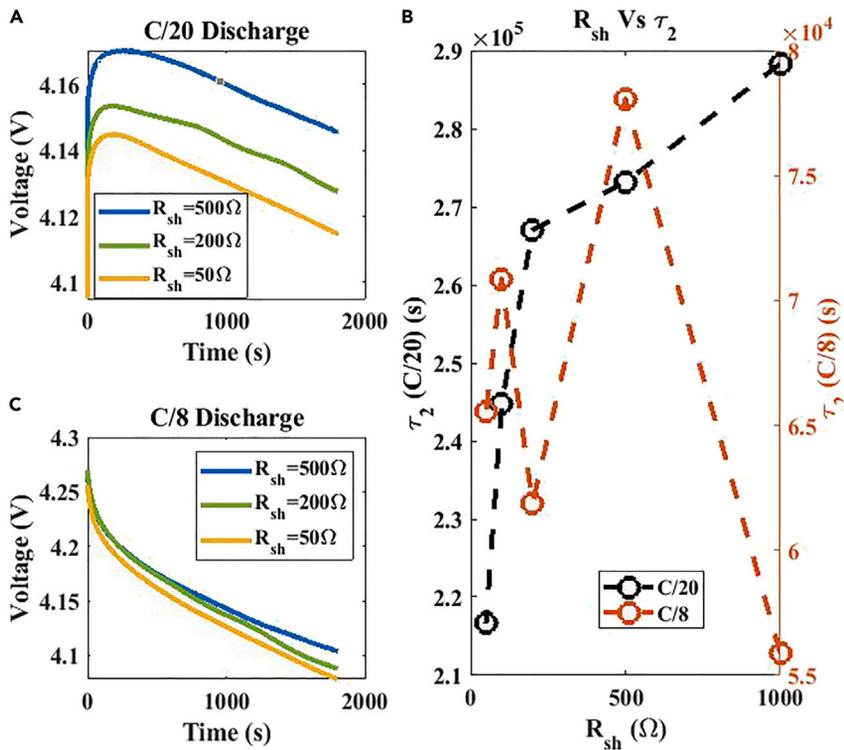
Figure 6. Exploring the c-rate limit for Short detection
Variation of Rest-Period/Open-Circuit Voltage profiles with time at two c-rates: (a) C/20 and (c) C/8 for different short resistances, R_{sh}, with the corresponding variation of (b) the time constant, τ_2, with short resistance, R_{sh}.

R_{sh} estimation with τ_2

Although we have established the influence of R_{sh} on τ_2 and the influence of factors like T, SOH, SOC, etc. on the same, the next question would be on how to estimate the severity of the short, the short resistance, R_{sh}, from the decrease in τ_2. For this, we refer back to Figure 3B, where the trend of τ_2 with R_{sh} is plotted for battery 1 at 32°C. Based on the trend seen, we can formulate a simple power-law relationship between τ_2 and R_{sh} as follows:

$$\tau_2 = aR_{sh}^b + c \rightarrow R_{sh} = \left[\frac{\tau_2 - c}{a}\right]^{\left(\frac{1}{b}\right)} \qquad \text{(Equation 17)}$$

In Equation 17, parameters a, b, and c are fit to the curve seen in Figure 3B. As explained earlier in the methods section, 4500 charge-discharge cycles and rest period data were generated (300 cycles for every 3 temperatures [T = 18°C, 23°C, 32°C] & 5 short resistances [R_{sh} = 50Ω-100Ω-200Ω-500Ω- ∞ Ω]). Rest period from these is used for short resistance prediction using Equation 17. A few sets of evaluation are shown in Figure 7 below, and the rest are shown in Figure S8 of the supplementary information. The predicted $R_{sh,predicted}$, as per Equation 17, as a function of the cycle number, for a particular T- R_{sh} pair is shown in these figures. The summary of the predictions for different combinations of the actual short resistance used in the experiments, R_{sh}, and the ambient temperature, T, is shown in Table 1 below. The mean R_{sh} is the mean of all the R_{sh} predictions over 300 cycles of the data (or until the cycle number for which SOH >85%, whichever is earlier), and the prediction variation is also shown in the column with the standard deviation. The mean R_{sh} and the estimation error are defined as follows:

$$R_{sh,mean} = \frac{1}{n}\sum_{n=1}^{n=m} R_{sh,predicted} \; ; \; Error \; (\%) = \left[\frac{\left|R_{sh} - R_{sh,mean}\right|}{R_{sh}}\right] \times 100 \qquad \text{(Equation 18)}$$

Where $R_{sh,predicted}$ is the predicted R_{sh} for the particular cycle number, n, using Equation 17 and m = 300 or the cycle number until which SOH ≥85%. For the healthy case, or $R_{sh} = \infty$Ω, the estimation error is considered to be zero, as long as the predicted R_{sh} is >700Ω. The prediction accuracy is very good considering
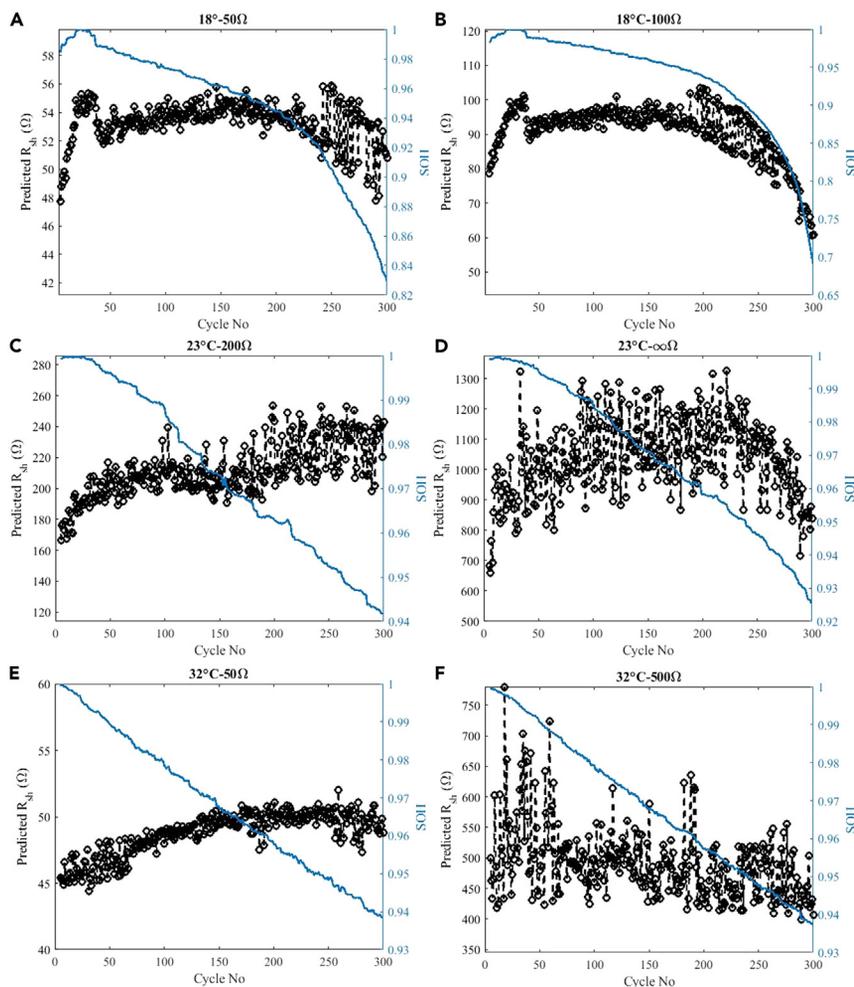
Figure 7. Validation with Experimental data

Panels (A-F) show the variation of predicted short resistance, R_{sh}, using the model, with cycle number along with the SOH profile for various values of the actual short resistance, R_{sh}, used in experiments and ambient temperature, T. The T-R_{sh} values used in experiments are indicated in the title of each panel/sub-figure.

that the method is able to distinguish soft short of different severities (50Ω–500Ω) very well. The literature shows that it is very difficult to differentiate a cell with a soft short of $R_{sh} \geq 100\Omega$ from a healthy cell as the soft-short influence is very minimal to show up as anything significant on battery states.[9,24,48] However, the feature used over here, which is the long-tail time constant, τ_2, is very sensitive to the different severities of a soft short, leading to early detection and precise estimation.

Although the method does not rely on the cycle number/SOH as such for the predictions, the variation of the SOH with cycle number is also plotted in Figure 7. Equation 17 being SOH agnostic, it is interesting to see how the predictions may be improved by considering a simple scaling of the R_{sh} predictions, with the SOH, when the SOH is below 85%. This is seen in Figure 8B; the R_{sh} prediction profile follows the SOH variation, when the SOH is below 85%. But, as mentioned earlier, batteries are usually discarded for second life use, when the SOH drops below 80%. In any case, it may be worth considering this aspect as an improvement to the method, whereby the predictions for SOH <85% are done by considering the SOH as well, which is a readily available metric.

It is quite interesting to notice that the SOH drops quite fast at lower temperatures and at higher short resistances as seen in Figures 7 and S8 of the supplementary information. The possible reason for this could be due to the phenomenon of lithium plating, whose formation is accelerated at low temperatures and high

Table 1. Table showing the short resistance prediction for different actual R_{sh}-Temperature T pair

S.I. No	Temperature (C)	Actual R_{sh} (Ω)	Predicted Mean R_{sh} (Ω)	Standard Deviation (Ω)	Estimation Error (%)
1	18	50	51.3	1.4	2.6
2	18	100	90.9	3.6	9.1
3	18	200	180.5	19.3	9.7
4	18	500	443.1	35.0	11.4
5	18	∞	713.1	83.9	0
6	23	50	48.6	1.0	2.8
7	23	200	211.6	15.1	5.8
8	23	500	435.4	37.5	12.9
9	23	∞	1036.1	127.4	0
10	32	50	48.8	1.6	2.5
11	32	100	106.3	5.7	6.3
12	32	200	216.2	13.8	8.1
13	32	500	491.1	58.1	1.8
14	32	∞	1661.5	200.1	0

currents.[10–12,49] Also, the degradation is less in the presence of an SC as the short-induced leakage current would reduce the amount of time spent in the high-voltage windows (where the degradation is accelerated and amplified), leading to less severe impact on the cell. This explains the higher SOH with harder short (like 50Ω) causing lesser harm than softer short (like 500Ω) or no short at all. In any case, this is an interesting observation, however outside the scope of the present study to address it further.

Application for pack architecture

Although the method has been shown to work under different conditions of temperature, aging, etc., the configuration considered until now is that of a single cell. Most of the applications involving LIBs use pack-like EVs. Thus, it would be interesting to see how the method will work on such form factors. To answer this question, three batteries of the type battery 3, with a capacity of 4Ah, were connected in series. The individual voltage was roughly around 2.9V–3.0V (almost fully discharged). The reason behind connecting these cells in series is to replicate a real-time scenario. Battery packs usually have modules (cells connected in series), and these modules are connected in parallel to form the battery pack depending on the voltage and capacity rating necessary. The voltage across modules, which are connected in parallel, will remain the same, with sensors and data available across these modules. Thus, we wanted to mimic the same condition by measuring the voltage across a module, which, in this case are three cells connected in series.

This module was subjected to the same experimental conditions as explained earlier in the methods section, with the rest-period voltage data being collected with an external short of different short resistances, R_{sh} (50Ω–500Ω), being connected across the terminals of one of the batteries in the module, throughout the experiments. The rest-period voltage profile is as shown in Figure 8A, and the time constant, τ_2, profile with R_{sh} is shown in Figure 8B. The profile is very similar to the profile for the individual cell of battery 3, shown in Figure S7B of the supplementary information, showing the applicability of this method across single cell and multi-cell geometries. Although we have not performed additional validations in this case, the intent here was to show the validity of this method, in detecting very early stages of short with a feature, which is highly sensitive to easily differentiate between different severities of the soft-short spectra.

Device implementation & perspectives

As elaborated earlier, the proposed framework is very easy for device implementation, hardly requiring any computations resources. The only inputs are the OCV/voltage data of 30 min duration (with a 1s resolution) at reference conditions and some basic mathematical operations. Also, as this method is highly sensitive to short severities of different magnitudes, a continuous tracking of the short resistance is possible with excellent accuracies. Apart from the method being free of any onboard ECT models, it is also chemistry independent. For example, battery electrodes are composed of materials which have diffusivities in the range
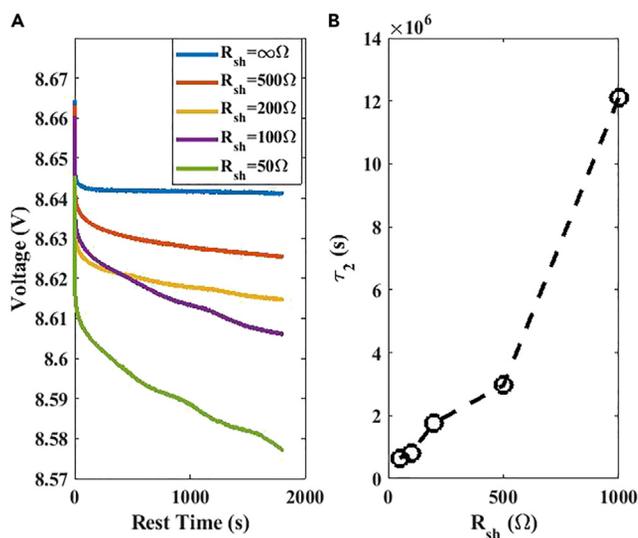
Figure 8. Short Detection on a Battery Module/Pack
Variation of (A) Rest-Period/Open-Circuit Voltage profiles with time for the pack configuration at different short resistances, R_{sh}, with the corresponding (B) variation of the time constant, τ_2, with short resistance, R_{sh}.

of 10^{-12}–10^{-15} m^2/s^2, which has a direct bearing on the time constant τ_2 as shown in Figure 9 below. As the method relies on measuring τ_2 and its deviation from the reference value, it addresses all the variables of battery chemistry, active material particle radii, form factor, etc., to become a very generic method. Apart from being implemented on BMS toward on-device safety assessment, it can also be integrated as part of protocols employed during battery manufacturing, quality checks, and at service centers, to detect and isolate faulty cells.

Conclusions

In this study, we have introduced a new and effective method to detect very early stage of LIB SC and estimate the short resistance with notable precision. The rest-period voltage is characterized by an exponential decay/rise in the voltage, saturating to a steady-state value in the long term due to diffusion-dominated equilibration of concentration inside the active electrode solid particles. The proposed DE model and its time constants, τ_1 & τ_2, capture the two distinct stages of this behavior. The long-term voltage saturation and its time constant, τ_2, are influenced by small leakage currents associated with SCs. This is due to the observation that time constants associated with an early-stage/soft short ($R_{sh} \geq 50\Omega$) overlap with the time constant, τ_2, of the voltage relaxation, leading to an intertwining of these processes. Thus, by measuring the long-term relaxation (or decay) time constant, τ_2, and its decrease as compared to that of a healthy cell, one can detect SCs and estimate the short resistance, R_{sh}, respectively. This observation was validated with experiments, where commercial mobile phone batteries of NG-LCO chemistry were induced with an external short of varying resistance in the soft-short range. The prediction accuracy was excellent (<10% error), and the method was able to factor in the influence of important variables like battery capacity, temperature, SOC, and SOH. The feature used via the long-tail time constant, τ_2, is unique and is applicable across batteries of different form factors and chemistries that involve solid-state diffusion. Moreover, it is highly sensitive to different severities of short and can easily distinguish between them. With negligible computational requirements, the method can be easily integrated on any BMS, offering a neat, precise, and robust early-stage short detection and estimation algorithm, which is the need of the hour in the ever-evolving battery domain.

Limitations of study

Apart from discussing the details and usefulness of the proposed approach, it is also important to understand some of the underlying assumptions and discuss the pros and cons as well. One of the requirements for this protocol to work effectively is to make sure that the data (OCV or low c-rate voltage) are collected at the same reference SOC points (e.g., after the CV phase of charging or at 90% SOC etc.). It is also expected
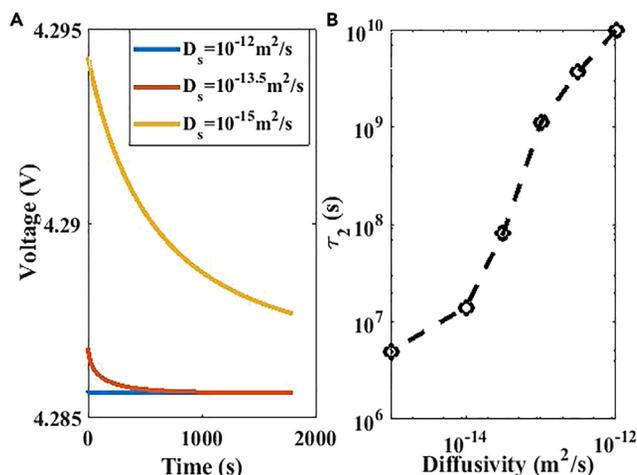
Figure 9. τ_2 for different materials/diffusivities

Variation of (A) Rest-Period/Open-Circuit Voltage profiles with time for different diffusivities, D_s, with the corresponding variation of (B) the time constant, τ_2, with Diffusivity, D_s.

that the PMIC will have the reference (healthy cell) τ_2 value(s) at the trigger SOC(s) of evaluation so that the deviation from the same will be used for estimating the R_{sh}. Although the protocol is SOH agnostic, we notice that below an SOH of 85%, the model needs to include the SOH value itself, through a simple scaling, to improve the prediction accuracy. Cells are usually retired for a second life use especially for storage applications below an SOH of 80%, and thus including the SOH aspect can boost the applicability of this approach. The OCV/voltage data duration requirement of 30 min is one more requirement. We realize that, to measure the long-tail time constant of τ_2 and to differentiate it from SC-influenced profiles, a minimum of 30 min is necessary; although data of longer duration are always welcome. Another assumption while working out this approach is that the short is a persistent one. For SCs, which are intermittent, the method may need to be modified to account for the specific condition. For example, it is known that dendrite formation and many other short-inducing phenomena are usually triggered at very high/low SOCs; it is recommended to apply this protocol at such SOC windows.

STAR★METHODS

Detailed methods are provided in the online version of this paper and include the following:

- KEY RESOURCES TABLE
- RESOURCE AVAILABILITY
  - Lead contact
  - Materials availability
  - Data and code availability
- EXPERIMENTAL MODEL AND SUBJECT DETAILS
- METHOD DETAILS
- QUANTIFICATION AND STATISTICAL ANALYSIS
- ADDITIONAL RESOURCES

SUPPLEMENTAL INFORMATION

Supplemental information can be found online at https://doi.org/10.1016/j.isci.2023.106636.

ACKNOWLEDGMENTS

AUTHOR CONTRIBUTIONS

S.B. & S.P.A. conceived the idea and came up with the framework. SB designed the modeling work, analyzed the data, and made the figures. M.J. performed the experiments and provided the experimental

data. S.B. & S.P.A. wrote the paper. K.S.M. and J.K. gave constructive inputs and edits to the manuscript. All the authors discussed the results and commented on the manuscript at all stages.

DECLARATION OF INTERESTS

The authors declare no competing interests.

INCLUSION AND DIVERSITY

We support inclusive, diverse, and equitable conduct of research.

REFERENCES

1. Kato, H., Yamamoto, Y., Nagamine, M., and Nishi, Y. (1993). Lithium Ion Rechargeable Batteries (WESCON).

2. Hariharan, K.S., Tagade, P., and Ramachandran, S. (2018). Mathematical Modeling of Lithium Batteries from Electrochemical Models to State Estimator Algorithms (Springer).

3. Feng, X., Ouyang, M., Liu, X., Lu, L., Xia, Y., and He, X. (2018). Thermal runaway mechanism of lithium ion battery for electric vehicles: a review. Energy Storage Mater. 10, 246–267.

4. Feng, X., Ren, D., He, X., and Ouyang, M. (2020). Mitigating thermal runaway of lithium-ion batteries. Joule 4, 743–770.

5. Kolly, J., Panagiotou, J., and Czech, B. (2013). The Investigation of a Lithium-Ion Battery Fire Onboard a Boeing 787 by the US National Transportation Safety Board (Dothan,, AL, USA: Saf. Res. Corp. Amer.).

6. Samsung News Room (2017). https://news.samsung.com/global/infographic-galaxy-note7-what-we-discovered.

7. Guo, R., Lu, L., Ouyang, M., and Feng, X. (2016). Mechanism of the entire overdischarge process and overdischarge-induced internal short circuit in lithium ion batteries. Sci. Rep. 6, 30248.

8. Huang, L., Liu, L., Lu, L., Feng, X., Han, X., Li, W., Zhang, M., Li, D., Liu, X., Sauer, D.U., and Ouyang, M. (2021). A review of the internal short circuit mechanism in lithium-ion batteries: inducement, detection and prevention. Int. J. Energy Res. 45, 15797–15831.

9. Bharathraj, S., Adiga, S.P., Kaushik, A., Mayya, K., Lee, M., and Sung, Y. (2022). Towards in-situ detection of nascent short circuits and accurate estimation of state of short in Lithium-Ion Batteries. J. Power Sources 520, 230830–230910.

10. Bhattacharyya, R., Key, B., Chen, H., Best, A.S., Hollenkamp, A.F., and Grey, C.P. (2010). in-situ NMR observation of the formation of metallic lithium microstructures in lithium batteries. Nat. Mater. 9, 504–510.

11. Harry, K.J., Hallinan, D.T., Parkinson, D.Y., MacDowell, A.A., and Balsara, N.P. (2014). Detection of subsurface structures underneath dendrites formed on cycled lithium metal electrodes. Nat. Mater. 13, 69–73.

12. Jana, A., Woo, S.I., Vikrant, K.S.N., and García, R.E. (2019). Electrochemomechanics of lithium dendrite growth. Energy Environ. Sci. 12, 3595–3607.

13. Lai, X., Jin, C., Yi, W., Han, X., Feng, X., Zheng, Y., and Ouyang, M. (2021). Mechanism, modelling, detection and prevention of the internal short circuit in lithium-ion batteries: recent advances and perspectives. Energy Storage Mater. 35, 470–499.

14. Orendorff, C.J., Roth, E.P., and Nagasubramanian, G. (2011). Experimental triggers for internal short circuits in lithium-ion cells. J. Power Sources 196, 6554–6558.

15. Seo, M., Park, M., Song, Y., and Kim, S.W. (2020). Online detection of soft internal short circuit in lithium-ion batteries at various standard charging ranges. IEEE Access 8, 70947–70959.

16. Kong, X., Plett, G.L., Trimboli, M.S., Zhang, Z., Qiao, D., Zhao, T., and Zheng, Y. (2020). Pseudo-two-dimensional model and impedance diagnosis of micro internal short circuit in lithium-ion cells. J. Energy Storage 27, 101085.

17. Kim, J.G., Son, B., Mukherjee, S., Schuppert, N., Bates, A., Kwon, O., Choi, M.J., Chung, H.Y., and Park, S. (2015). A review of lithium and non-lithium based solid state batteries. J. Power Sources 282, 299–322.

18. Naguib, M., Allu, S., Simunovic, S., Li, J., Wang, H., and Dudney, N.J. (2018). Limiting internal SC damage by electrode partition for impact-tolerant Li-ion batteries. Joule 2, 155–167.

19. Wu, H., Zhuo, D., Kong, D., and Cui, Y. (2014). Improving battery safety by early detection of internal shorting with a bifunctional separator. Nat. Commun. 5, 5193–5196.

20. Seo, M., Goh, T., Park, M., and Kim, S. (2018). Detection method for soft internal hort circuit in lithium-ion battery pack by extracting open circuit voltage of faulted cell. Energies 11, 1669–1680.

21. Li, X., Wang, Z., Liu, J.Y., Mao, Y.D., Huang, J., Wang, W., and Ma, X. (2018). Novel fault diagnosis method for lithium-ion battery packs of electric vehicles. Measurement 116, 402–411.

22. Ouyang, M., Zhang, M., Feng, X., Lu, L., Li, J., He, X., and Zheng, Y. (2015). Internal short circuit detection for battery pack using equivalent parameter and consistency method. J. Power Sources 294, 272–283.

23. Xia, B., Shang, Y., Nguyen, T., and Mi, C. (2017). A correlation based fault detection method for short circuits in battery packs. J. Power Sources 337, 1–10.

24. Naha, A., Khandelwal, A., Hariharan, K.S., Kaushik, A., Yadu, A., and Kolake, S.M. (2019). On-board SC detection of Li-ion batteries undergoing fixed charging profile as in smartphone applications. IEEE Trans. Ind. Electron. 66, 8782–8791.

25. Naha, A., Khandelwal, A., Agarwal, S., Tagade, P., Hariharan, K.S., Kaushik, A., Yadu, A., Kolake, S.M., Han, S., and Oh, B. (2020). Internal short circuit detection in Li-ion batteries using supervised machine learning. Sci. Rep. 10, 1301–1312.

26. Sidhu, A., Izadian, A., and Anwar, S. (2015). Adaptive nonlinear model-based fault diagnosis of lithium ion batteries. IEEE Trans. Ind. Electron. 62, 1002–1011.

27. Plett, G.L. (2004). Extended Kalman filtering for battery management systems of LiPB-based HEV battery packs. J. Power Sources 134, 252–261.

28. Wu, X., Li, X., and Du, J. (2018). State of charge estimation of lithium-ion batteries over wide temperature range using unscented Kalman filter. IEEE Access 6, 41993–42003.

29. Chen, W., Chen, W., Saif, M., Li, M., and Wu, H. (2014). Simultaneous fault isolation and estimation of lithium-ion batteries via synthesized design of Luenberger and

learning observers. IEEE Trans. Control Syst. Technol. *22*, 290–298.

30. Bharathraj, S., Lee, M., Adiga, S.P., Song, T., Mayya, K.S., and Kim, J.H. (2023). Detection, classification and quantification of short circuits in batteries using a short fatigue metric. J. Energy Storage *61*, 106729–10672912.

31. Farmann, A., and Sauer, D.U. (2017). A study on the dependency of the open-circuit voltage on temperature and actual aging state of lithium-ion batteries. J. Power Sources *347*, 1–13.

32. Barai, A., Uddin, K., Widanage, W.D., McGordon, A., and Jennings, P. (2018). A study of the influence of measurement timescale on internal resistance characterisation methodologies for lithium-ion cells. Sci. Rep. *8*, 21.

33. Doyle, M., Newman, J., Gozdz, A.S., Schmutz, C.N., and Tarascon, J. (1996). Comparison of modeling predictions with experimental data from plastic lithium ion cells. J. Electrochem. Soc. *143*, 1890–1903.

34. Bharathraj, S., Kaushik, A., Adiga, S.P., Kolake, S.M., Song, T., and Sung, Y. (2021). Accessing the current limits in lithium ion batteries: analysis of propensity for unexpected power loss as a function of depth of discharge, temperature and pulse duration. J. Power Sources *494*, 229723–22972310.

35. Jiang, F., and Peng, P. (2016). Elucidating the performance limitations of lithium-ion batteries due to species and charge transport through five characteristic parameters. Sci. Rep. *6*, 32639–3263910.

36. Zhu, J., Zhang, X., Sahraei, E., and Wierzbicki, T. (2016). Deformation and failure mechanisms of 18650 battery cells under axial compression. J. Power Sources *336*, 332–340.

37. Li, W., Xia, Y., Zhu, J., and Luo, H. (2018). State-of-Charge dependence of mechanical response of lithium-ion batteries: a result of internal stress. J. Electrochem. Soc. *165*, A1537–A1546.

38. Yuan, C., Wang, L., Yin, S., and Xu, J. (2020). Generalized separator failure criteria for internal short circuit of lithium-ion battery. J. Power Sources *467*, 228360–22836010.

39. Weppner, W., and Huggins, R.A. (1977). Determination of the kinetic parameters of MixedConducting electrodes and application to the system Li3Sb. J. Electrochem. Soc. *124*, 1569–1578.

40. Pop, V., Bergveld, H.J., Regtien, P.P.L., Op het Veld, J.H.G., Danilov, D., and Notten, P.H.L. (2007). Battery aging and its influence on the electromotive force. J. Electrochem. Soc. *154*, 744–750.

41. Valøen, I., and Reimers, J. (2005). Transport properties of LiPF6-based Li-ion battery electrolytes. J. Electrochem. Soc. *152*, 882–890.

42. Barré, A., Deguilhem, B., Grolleau, S., Gérard, M., Suard, F., and Riu, D. (2013). A review on lithium-ion battery ageing mechanisms and estimations for automotive applications. J. Power Sources *241*, 680–689.

43. Bharathraj, S., Adiga, S.P., Patil, R.S., Mayya, K.S., Song, T., and Sung, Y. (2019). An efficient and chemistry independent analysis to quantify resistive and capacitive loss

contributi ons to battery degradation. Sci. Rep. *9*, 6576–657610.

44. Bharathraj, S., Adiga, S.P., Mayya, K.S., Song, T., Kim, J., and Sung, Y. (2020). Degradation-guided optimization of charging protocol for cycle life enhancement of Li-ion batteries with Lithium Manganese Oxide-based cathodes. J. Power Sources *474*, 228659–228670.

45. Mandli, A.R., Kaushik, A., Patil, R.S., Naha, A., Hariharan, K.S., Kolake, S.M., Han, S., and Choi, W. (2019). Analysis of the effect of resistance increase on the capacity fade of lithium ion batteries. Int. J. Energy Res. *43*, 2044–2056.

46. Santhanagopalan, S., Guo, Q., Ramadass, P., and White, R.E. (2006). Review of models for predicting the cycling performance of lithium ion battehries. J. Power Sources *156*, 620–628.

47. Huang, S.C., Tseng, K.H., Liang, J.W., Chang, C.L., and Pecht, M. (2017). An online SOC and SOH estimation model for lithium-ion batteries. Energies *10*, 512.

48. Seo, M., Goh, T., Park, M., Koo, G., and Kim, S. (2017). Detection of internal short circuit in lithium ion battery using model-based switching model method. Energies *10*, 76–89.

49. Tippmann, S., Walper, D., Balboa, L., Spier, B., and Bessler, W.G. (2014). Low-temperature charging of lithium-ion cells part I: electrochemical modeling and experimental investigation of degradation behavior. J. Power Sources *252*, 305–316.

STAR★METHODS

KEY RESOURCES TABLE

REAGENT or RESOURCE	SOURCE	IDENTIFIER
Software and algorithms		
MATLAB Version 9.6 (R 2019a)	The MathWorks Inc.	https://www.mathworks.com
Curve Fitting Toolbox MATLAB Version 3.5.9 (R 2019a)	The MathWorks Inc.	https://www.mathworks.com

RESOURCE AVAILABILITY

Lead contact

Further information and requests for resources and reagents should be directed to and will be fulfilled by the lead contact, Sagar Bharathraj (s.bharathraj@samsung.com).

Materials availability

This study did not generate new unique reagents.

Data and code availability

- The battery data reported in this study cannot be deposited in a public repository because it is confidential in nature and is a property of the company, where the authors are employees.
- This paper does not report original code.
- Any additional information required to reanalyse the data reported in this paper, will be considered for sharing by the lead contact upon request.

EXPERIMENTAL MODEL AND SUBJECT DETAILS

Not relevant to this study.

METHOD DETAILS

There were both experiments and simulations performed as part of this study. The experiments were performed on three different types of NG-LCO commercial batteries, each with a nominal voltage of 3.85V and capacities of 1.85Ah, 4Ah and 4.85Ah. The P2D simulations were performed using MATLAB and run on an Intel (R) Core (TM) i7-6700HQ CPU @ 2.6 GHz, 8GB RAM. More details are provided in the methods of this study.

QUANTIFICATION AND STATISTICAL ANALYSIS

Not relevant to this study.

ADDITIONAL RESOURCES

Not relevant to this study.